Numerical Analysis of Bladed Disk–Casing Contact With Friction and Wear

Patricio Almeida, Claude Gibert, Fabrice Thouverez, Xavier Leblanc, Jean-Philippe Ousty

Numerical Analysis of Bladed Disk–Casing Contact With Friction and Wear

P. Almeida[1]
SAFRAN Turbomeca, Avenue Joseph Szydlowski, Bordes Cedex 64511, France

C. Gibert, F. Thouverez, X. Leblanc
Ecole Centrale de Lyon, Laboratoire de Tribologie et Dynamique des Systèmes,
36 Avenue Guy de Collongue, Ecully, France

J.-P. Ousty
SAFRAN Turbomeca, Avenue Joseph Szydlowski, Bordes Cedex 64511, France

In order to increase the aerodynamic performances of their engines, aircraft engine man-ufacturers try to minimize the clearance between rotating and stationary parts in axial and centrifugal compressors. Consequently, the probability of contact increases, leading to undesirable phenomena caused by forced excitation of the natural modes or by modal interaction. Due to the complexity of these phenomena, many numerical studies have been conducted to gain a better understanding of the physics associated with them, look-ing primarily at their respective influence on potential unstable behaviors. However, the influence of other physical phenomena, such as friction and wear, remains poorly under-stood. The aim of this work is to show some effects associated with friction and wear on the dynamic behavior resulting from blade-to-casing interaction. The numerical study reported here is based on a simplified finite element model of a rotating bladed disk and a flexible casing. The contact algorithm uses an explicit time marching scheme with the Lagrange multipliers method. Friction and wear are formulated using, respectively, Cou-lomb's and Archard's laws. The rotational speed is set to critical speed giving rise to modal interaction between a backward mode of the casing and a counter-rotating mode of the bladed disk with one nodal diameter (ND). Contact is initiated by a dynamic exci-tation of the stator. In the presence of friction, the system becomes unstable when a side-band of the excitation frequency coincides with 1ND mode of the bladed disk. The introduction of wear leads to a vibration reduction, while the abradable material is removed by the wear process. The number of wear lobes produced on the casing is related to the ratio between the vibration frequency of the blades and the rotating speed. The ratio obtained by means of the FE model corroborates experimental observations.

Keywords: blade–casing contact, abradable coating, wear, spectral analysis, traveling waves

Introduction

In helicopter and aircraft engines, the contact between blade tips and surrounding casings is now commonly accepted as a part of normal engine operation. In order to mitigate the severity of contact, abradable coatings are thermally sprayed on the engine casings. Nevertheless, in some specific conditions the contact may lead to high dynamic excitations or even to unstable vibrations on both structures. Naturally, mastering blade-to-casing interactions is a priority for turbomachinery manufacturers. The compressor designers must predict the vibration behavior of the system taking into account the predominant physical phenomena. In this context, numerical and experimental investigations have been devoted to understanding the physical phenomena associated with contact and their respective influence on possible unstable behaviors [1]. Recent experimental research shows the significant dynamic response of a centrifugal compressor and its surrounding casing produced by a coincidence between the harmonics of the rotating speed and the natural modes of both structures [2]. The resulting spectral content of response is characterized by some sidebands aside the main excited frequency which may lead to the excitation of other frequency modes.

During contact, the processes of friction and wear influence the dynamic behavior of structures [2–4], thus making it necessary to establish the mathematical formulation of an elastodynamic contact problem with friction and wear, for subsequent application to a case of blade-to-casing interaction. Unilateral contact with friction is usually modeled through Coulomb's friction law, whereas wear can be introduced using the various approaches addressed by the literature as follows. Strömberg [5] and Salles et al. [6] modeled wear using Archard's law [7], while Williams [8] and Batailly et al. [4] proposed a plastic behavior law for the abradable coating. Within the scope of this paper, we will be using an Archard's law formulation because it provides an effective representation of the wearing problem, while remaining rather simple to integrate with the simulations. For interpretation of the references to color in this paper, the reader is referred to the web version of this article.

Dynamical Model

A finite element model of a bladed disk featuring contact against a flexible casing [9] has been implemented. The bladed disk model has six blades modeled by two Euler–Bernoulli beams per blade with six degrees-of-freedom per node. The disk is also modeled by Euler–Bernoulli beams that couple the blades, with two degrees-of-freedom per node: radial displacement and rotation along the axis of the rotational speed.

The casing is modeled by a continuous elastic ring [10] containing two degrees-of-freedom at every point, i.e., radial displacement $u_s(\theta, t)$ and tangential displacement $w_s(\theta, t)$ at the middle plane. Figure 1 shows the dynamical model used here. θ is an angular coordinate around the casing. Ring displacements are expressed through the use of Ritz functions, in accordance with the procedure described by Love [11]

$$w_s(\theta, t) = \sum_{n_d=1}^{k_{\text{tot}}} A^{n_d}(t)\cos(n_d\,\theta) + B^{n_d}(t)\sin(n_d\,\theta) \qquad (1)$$

[1]Corresponding author.

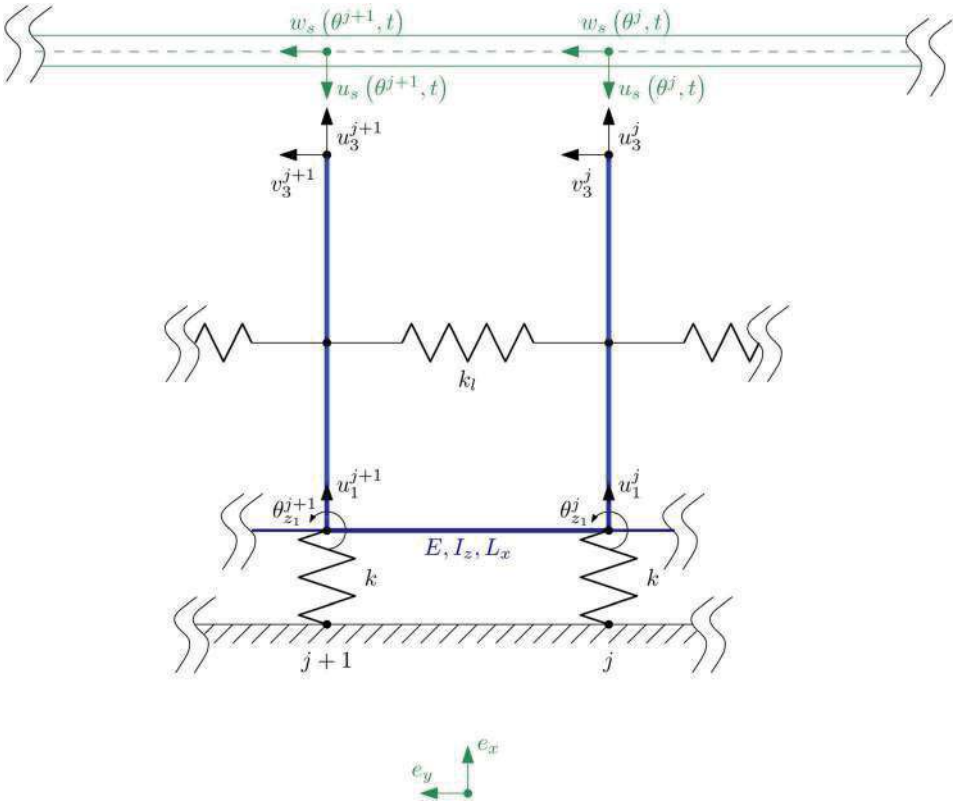

Fig. 1 Schematic of two sectors of the bladed disk with the elastic ring (casing)

where k_{tot} is the number of NDs (or modes) taken into account. The ring is assumed to be inextensible, which implies that radial displacement is related to the tangential displacement [12]

$$u_s(\theta,t) = \frac{\partial w_s(\theta,t)}{\partial \theta} \tag{2}$$

The ring thus features $2k_{\text{tot}}$ degrees-of-freedom. Note that the condition (2) bans the modal shape of the casing with zero nodal diameter (0ND). The mass and stiffness matrices of the ring are derived by applying the Lagrange equations.

Furthermore, the mass and stiffness matrices of the bladed disk are obtained through a conventional finite element formulation. In this manner, solving the contact problem, with the inclusion of both the friction and wear phenomena, consists of solving the equations of motion of the bladed disk–casing system

$$\mathbf{M}\ddot{\mathbf{u}} + \mathbf{D}\dot{\mathbf{u}} + \mathbf{K}\mathbf{u} + \mathbf{F_c} = \mathbf{F_{ext}} \tag{3}$$

where $\mathbf{u}$ is the displacement vector, $\mathbf{M}$ is the mass matrix, $\mathbf{K}$ is the stiffness matrix, $\mathbf{D}$ is the structural damping matrix, $\mathbf{F_{ext}}$ is the external forces vector, and $\mathbf{F_c}$ is the contact forces vector which is obtained through the Lagrange multipliers method [13] as described below.

Contact Treatment

An explicit time step finite difference method is used to solve Eq. (3). The stability of an explicit scheme is provided for a time increment Δt smaller than a critical time increment Δt_{stab}. Following a convergence study, the time increment was set at a value 3 orders of magnitude smaller than the smallest characteristic period of the system. The (nonlinear) contact problem is solved by a succession of prediction/correction steps. These steps can be detailed as follows [14,15].

Prediction Step. The predicted[2] displacement vector $\mathbf{u}_{n+1,p}$ without taking into account contact forces is given by known values at previous times n and $n-1$

$$\mathbf{u}_{n+1,p} = \left[\frac{\mathbf{M}}{\Delta t^2} + \frac{\mathbf{D}}{2\Delta t}\right]^{-1} \left(\mathbf{F}_{\mathbf{ext}n} + \left(2\frac{\mathbf{M}}{\Delta t^2} - \mathbf{K}\right)\mathbf{u}_n + \left(\frac{\mathbf{D}}{2\Delta t} - \frac{\mathbf{M}}{\Delta t^2}\right)\mathbf{u}_{n-1}\right) \tag{4}$$

The initial distance between the two structures g must be updated using the predicted values, in order to verify Signorini's conditions relative to the unilateral contact. Wear is taken into account by applying a law similar to Archard's law [7] and then following the method described by Salles et al. [16–18] wherein wear is characterized by loss of matter and depends on normal contact pressure, tangential velocity, and wear rate—cf. Eq. (12). In this approach, wear is a variable which increases the initial gap between the two structures. The distance function $g(\mathbf{u}_N^M, \mathbf{w}^M)$ is dependent on relative normal displacement variables as well as wearing depth

$$g(\mathbf{u}_N^M, \mathbf{w}^M) = \mathbf{u}_N^M - \mathbf{w}^M - \mathbf{g}^M \tag{5}$$

where $\mathbf{u}_N^M$, $\mathbf{w}^M$, and $\mathbf{g}^M$ are, respectively, the relative normal displacement, wearing depth, and initial gap calculated on a set of contact points $\mathbf{x}^M$.

The contact occurs if $g(\mathbf{u}_N^M, \mathbf{w}^M)$ fails to satisfy the nonpenetration condition predicted during step $n+1$

$$g(\mathbf{u}_N^M, \mathbf{w}^M)_{n+1,p} \leq 0 \tag{6}$$

[2]The subscript p is used to declare the prediction step.

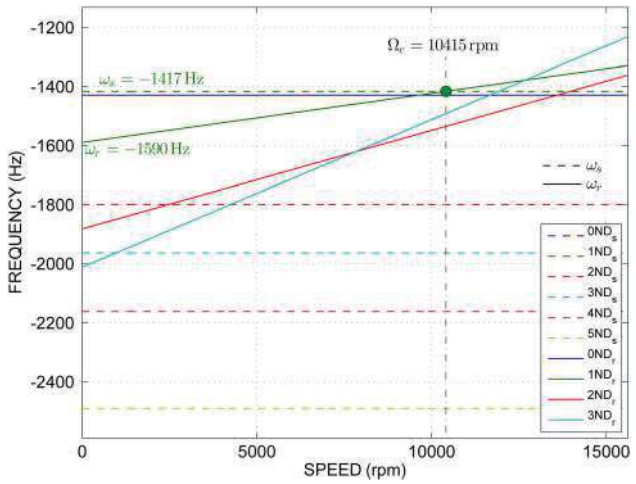

Fig. 2 Campbell diagram in stationary frame. Modal coincidence corresponds to the relation $-\omega_s^{n_d} = -\omega_r^{n_d} + n_d\,\Omega_c$.

The normal displacement vector in step $n+1$ is computed in the prediction step. Wear is calculated after the correction step—see Eq. (12)—since the normal contact force needs to be known first. The wearing depth vector value is introduced during step n in order to verify the nonpenetration conditions, expressed as follows:

$$\mathbf{u}^M_{Nn+1,p} - \mathbf{w}^M_n - \mathbf{g}^M \leq 0 \tag{7}$$

Correction Step. If according to the predicted values, the blade penetrates into the casing, a correction is applied to enforce the nonpenetration condition (8) as well as the force equilibrium condition (9)

$$g\left(\mathbf{u}^M_N, \mathbf{w}^M\right)_{n+1} = g\left(\mathbf{u}^M_N, \mathbf{w}^M\right)_{n+1,p} + {}^t\mathbf{C}_{\mathbf{N}n+1,p} \cdot \delta\mathbf{u}^M_{n+1} \tag{8}$$

$$\left(\frac{\mathbf{M}}{\Delta t^2} + \frac{\mathbf{D}}{2\Delta t}\right)\left(\mathbf{u}_{n+1} + \delta\mathbf{u}^M_{n+1}\right) = \mathbf{F}_{\mathbf{ext}n} + \mathbf{F}_{\mathbf{c}n+1} + \left(2\frac{\mathbf{M}}{\Delta t^2} - \mathbf{K}\right)\mathbf{u}_n + \left(\frac{\mathbf{D}}{2\Delta t} - \frac{\mathbf{M}}{\Delta t^2}\right)\mathbf{u}_{n-1} \tag{9}$$

where $\delta\mathbf{u}^M_{n+1}$ is the correction sought to validate both conditions, and $\mathbf{C_N}$ is the linearized vector yielding the normal force direction along with the displacement corrections direction. $\mathbf{F}_{\mathbf{c}n+1}$ is the vector of forces arising from the contact and may be expressed, leaving index $n+1$ for clarity, according to the Lagrange multipliers method by

$$\mathbf{F_c} = \mathbf{F}_{\mathbf{c}N} + \mathbf{F}_{\mathbf{c}T} = -[\mathbf{C_N} + \mathbf{C_T}]\lambda_N = -\mathbf{C_{NT}}\lambda_N \tag{10}$$

where $\mathbf{C_T}$ is the linearized vector yielding the friction force direction, and λ_N is the Lagrange multiplier. $\mathbf{C_T}$ is derived by using Coulomb's law during its sliding phase (permanent sliding). Thus, $\mathbf{C_T}$ depends on the coefficient of friction μ.

The system of equations resulting in $\lambda_{\mathbf{N}n+1}$ and $\delta\mathbf{u}^M_{n+1}$ still needs to be solved.

Finally, the Lagrange multipliers $\lambda_{\mathbf{N}n+1}$ and the correction vector $\delta\mathbf{u}^M_{n+1}$ are obtained as follows:

$$\begin{cases} \lambda_{\mathbf{N}n+1} = \left[\mathbf{C}^{\mathrm{T}}_{\mathbf{N}n+1,p}\left(\dfrac{\mathbf{M}}{\Delta t^2} + \dfrac{\mathbf{D}}{2\Delta t}\right)^{-1}\mathbf{C_{NT}}_{n+1,p}\right]^{-1}\mathbf{g}_{n+1,p} \\ \delta\mathbf{u}^M_{n+1} = -\left(\dfrac{\mathbf{M}}{\Delta t^2} + \dfrac{\mathbf{D}}{2\Delta t}\right)^{-1}\mathbf{C_{NT}}_{n+1,p}\lambda_{\mathbf{N}n+1} \end{cases} \tag{11}$$

At each time step n, the expressions for $\mathbf{g}_{n+1,p}$, $\mathbf{C}_{\mathbf{N}n+1,p}$, and $\mathbf{C_{NT}}_{n+1,p}$ are calculated on the basis of predicted values and with the accuracy required to ensure convergence.

Once the contact force calculation has been performed, we are able to calculate the wearing depth vector obtained by using the discretized Archard's law

$$\dot{\mathbf{w}}^M_{n+1} = k_w P_{Nn+1}\|\dot{\mathbf{u}}^M_{Tn+1}\| \tag{12}$$

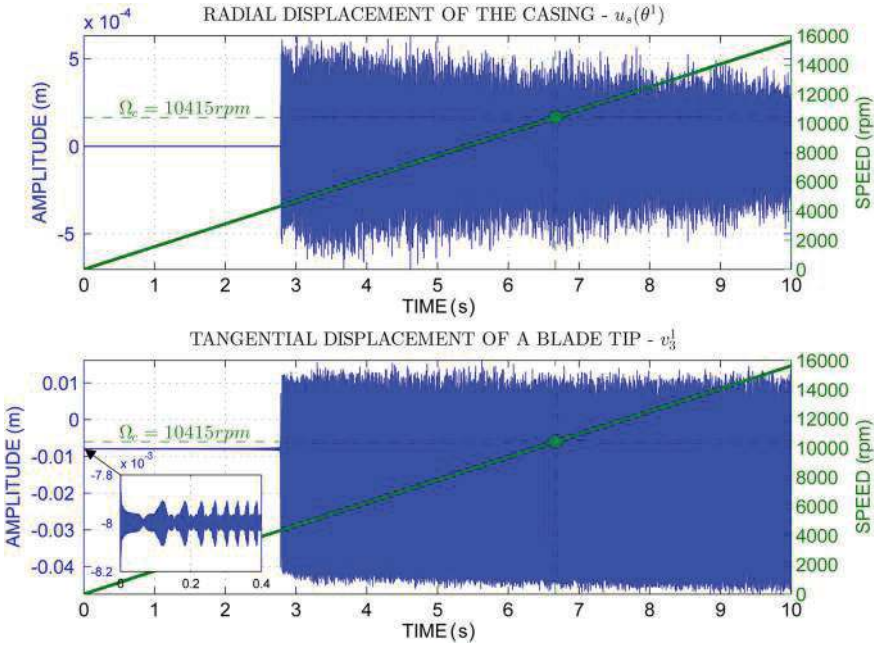

Fig. 3 Dynamic response of the casing (top) and the bladed disk (bottom) for $\mu = 0.1$ and $k_w = 0$

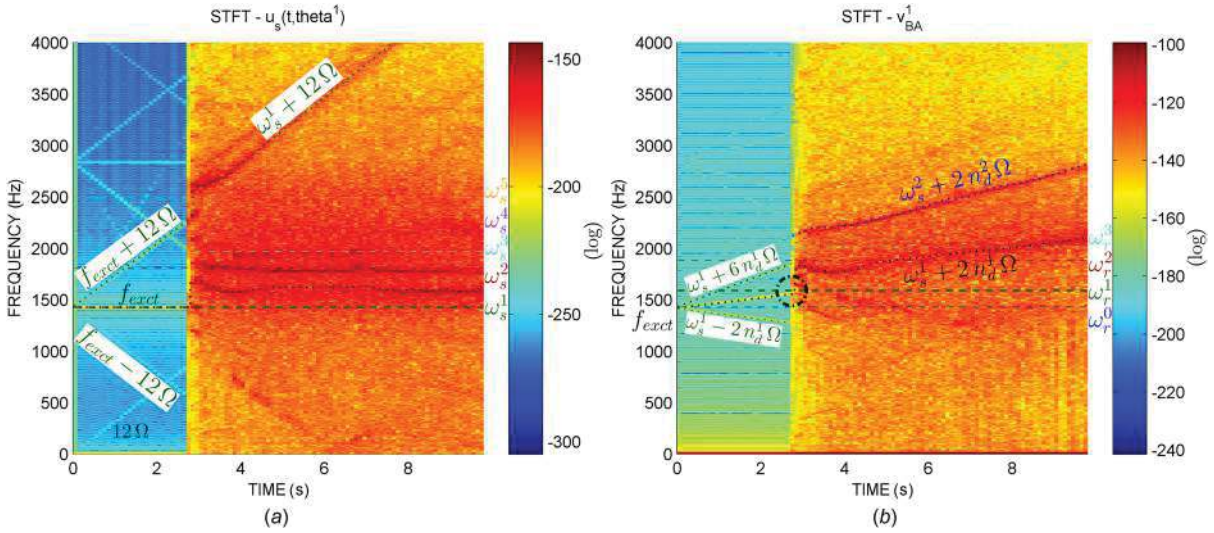

Fig. 4 STFT of the radial displacement of the casing and the tangential displacement of a blade tip for $\mu = 0.1$ and $k_w = 0$: (*a*) casing and (*b*) bladed disk

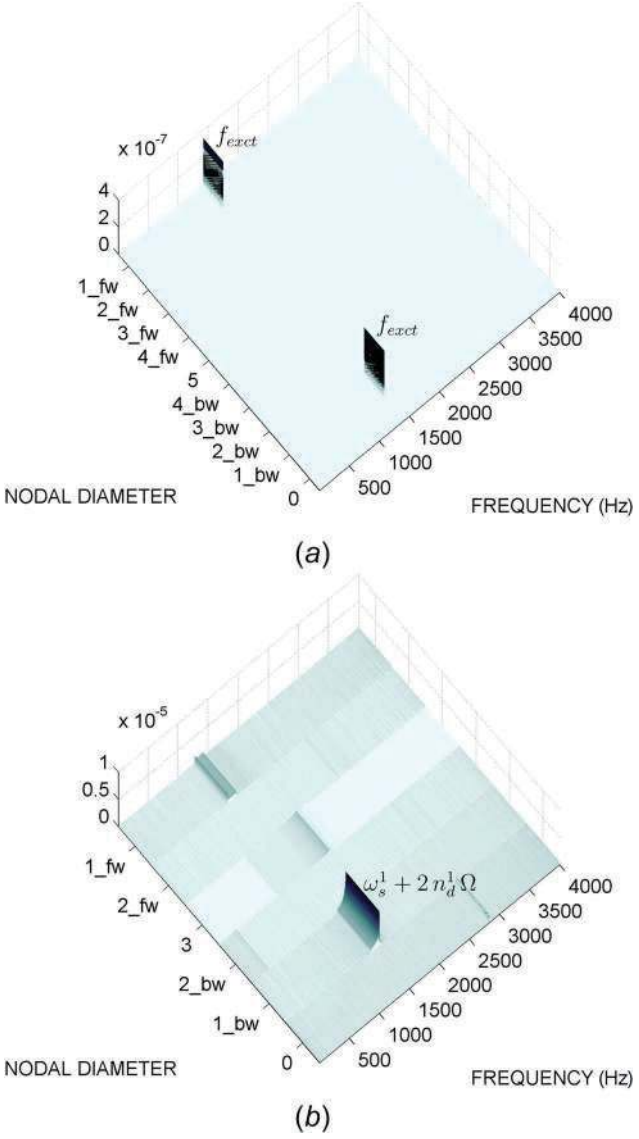

Fig. 5 Two-dimensional DFT diagram of the first family of modes of both structures at $t < 2.78$ s for $\mu = 0.1$ and $k_w = 0$: (*a*) casing and (*b*) bladed disk

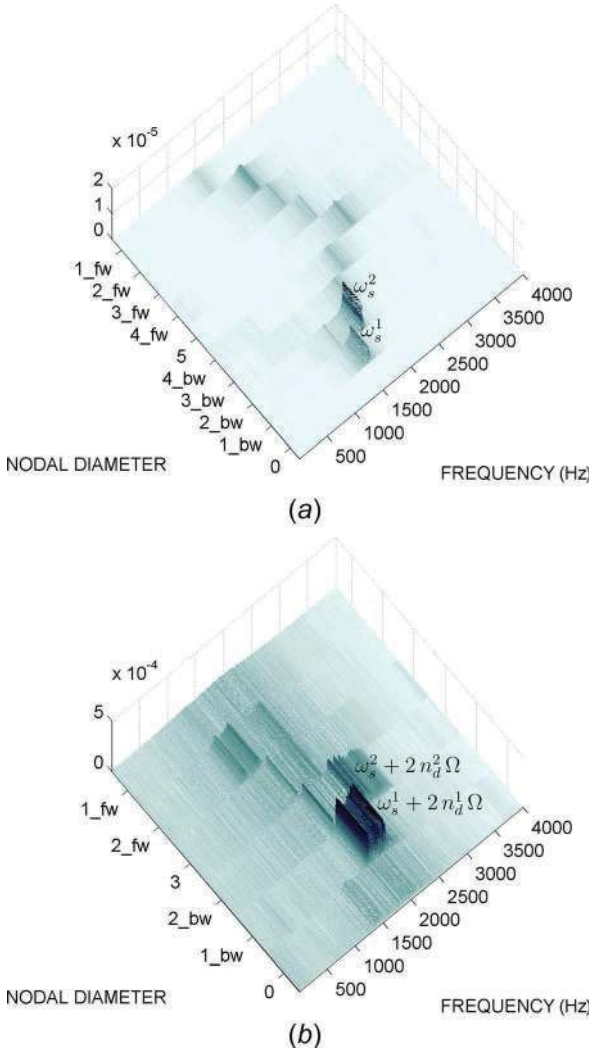

Fig. 6 Two-dimensional DFT diagram of the first family of modes of both structures at $t > 2.78$ s for $\mu = 0.1$ and $k_w = 0$: (*a*) casing and (*b*) bladed disk

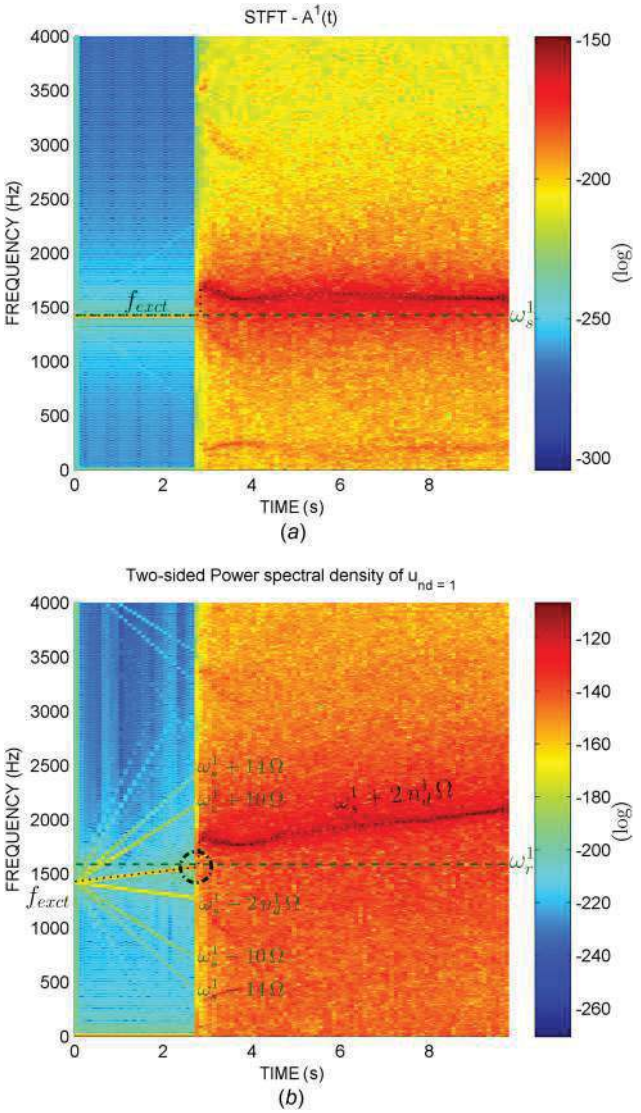

Fig. 7 Extraction of 1ND from STFT: (*a*) casing and (*b*) bladed disk

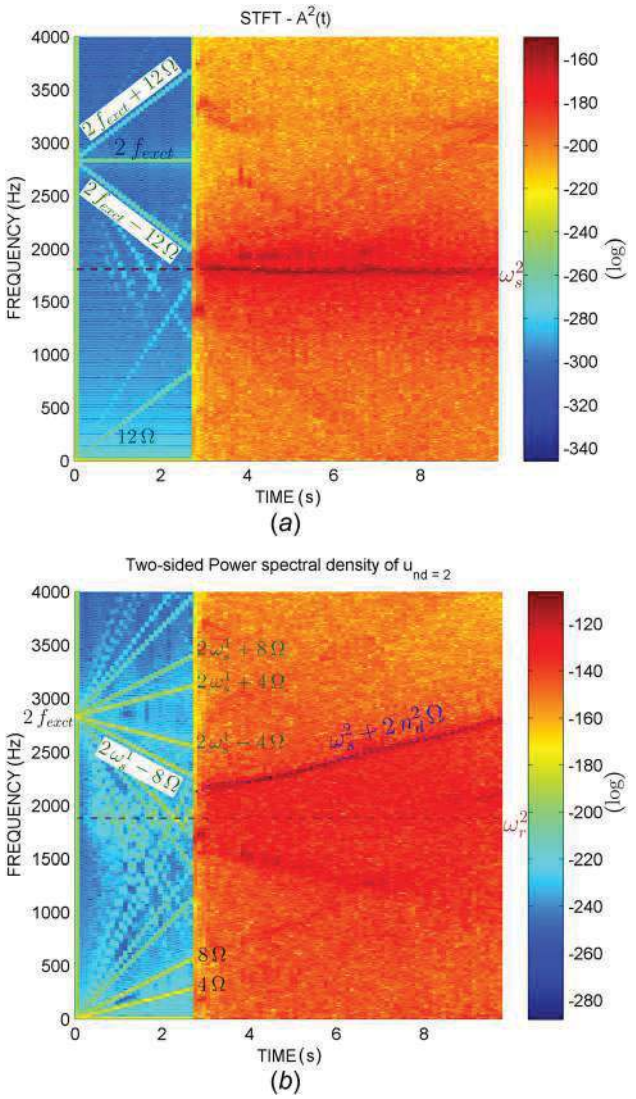

Fig. 8 Extraction of 2ND from STFT: (*a*) casing and (*b*) bladed disk

where k_w is the Archard's law wear coefficient, and P_N is the normal contact pressure.

Objectives

The main purpose of this paper is to study the dynamic behavior in a situation of blade-to-casing contact. A preliminary simulation including friction shows the dynamic behavior of structures. The results will be analyzed and compared to those of the same model including wear. The values of friction coefficient and Archard's wear coefficient have been chosen after a preliminary study presented in Ref. [9].

Contact is initiated by exciting a mode with 1ND on the stator with a stationary wave at $f_{\text{exct}} = \omega_s^1 = 1417$ Hz. The amplitude generated (1.5 μm) is sufficient to cover the clearance between the two structures (1 μm). The simulations were run for a rotational speed which follows a ramp passing through the critical speed for a modal interaction between a backward mode of the casing and a counter-rotating mode of the bladed disk with 1ND. The Campbell diagram of Fig. 2 highlights the critical velocity (at 10,415 rpm) for which a traveling wave speed coincidence (modal interaction) occurs [15,19] between the modes with 1ND of the two structures. In this case, modal interaction is said to occur when the natural frequency of the bladed disk coincides with the natural frequency of the casing, as expressed within the same frame [19]

$$-\omega_s^{n_d} = -\omega_r^{n_d} + n_d\,\Omega_c \tag{13}$$

with n_d as the number of NDs, ω_r as the natural frequency of the bladed disk mode with n_d nodal diameters, ω_s as the natural frequency of the casing mode with n_d nodal diameters, and Ω_c as the critical rotating speed.

Dynamic Behavior With Friction

A contact simulation with $\mu = 0.1$ and without wear ($k_w = 0$) is considered and will be compared to the simulations including wear in a second step.

Time Analysis. The time history of the dynamic response (see Fig. 3) shows transient event, characterized by a simultaneous increase in amplitude on both structures occurring about 2.78 s after the beginning of the simulation. This transient event will be called burst of vibration or shorter "burst" in this paper. The radial displacement of the casing reaches 600 μm, while the tangential

Table 1 Spatial and frequency content of the responses of both structures. Dotted lines denoted a frequency close to ω_s^1 (■■■■■), their sidebands (■■■■■), and a frequency which coincides with ω_s^2 (■■■■■)

	Casing		Bladed disk	
Spatial filtering	$t = [0–2.78]$ s	$t = [2.78–10]$ s	$t = [0–2.78]$ s	$t = [2.78–10]$ s
1ND	$f_{\text{excit}} = \omega_s^1$	■■■■■	$\omega_s^1 \pm 2\, n_d^1\, \Omega$ $\omega_s^1 \pm 10\, n_d^1\, \Omega$ $\omega_s^1 \pm 14\, n_d^1\, \Omega$	$\omega_s^1 \pm 2\, n_d^1\, \Omega$ (■■■■■)
2ND	$12\,\Omega$ $2 f_{\text{excit}}$ $2 f_{\text{excit}} \pm 12\,\Omega$	ω_s^2	$4\,\Omega$ $8\,\Omega$ $2\,\omega_s^1 \pm 4\, n_d^1\, \Omega$ $2\,\omega_s^1 \pm 8\, n_d^1\, \Omega$	$\omega_s^2 + 2\, n_d^2\, \Omega$ (■■■■■)
3ND	f_{excit} $f_{\text{excit}} \pm 12\,\Omega$	■■■■■ ■■■■■	$\omega_s^1 \pm 6\, n_d^1\, \Omega$	×
4ND	$12\,\Omega$ $2 f_{\text{excit}}$ $2 f_{\text{excit}} \pm 12\,\Omega$	 $\omega_s^2 - 11\,\Omega$ $\omega_s^2 + 12\,\Omega$	×	×
5ND	f_{excit} $f_{\text{excit}} \pm 12\,\Omega$	 ■■■■■	×	×

displacement of a particular blade tip exceeds $10{,}000\,\mu$m. Remember that the amplitude produced by the excitation on the elastic ring is $1.5\,\mu$m. In the figures, the speed ramp and the value of the critical speed are also provided. One can see that the burst of vibration starts before the critical speed corresponding to the modal coincidence.

After $t \approx 2.78$ s, the influence of the excitation is neglected (at $\Omega \approx 4350$ rpm). In order to confirm this assumption, another simulation (not presented here) was run by switching off the external excitation after $t = 3$ s. The results obtained are identical to those presented here. This clearly highlights the presence of a self-sustained vibration. Note that the dynamic response has an offset of -0.02 m, which corresponds to a static deflection in the opposite direction to the rotation of the blades.

Frequency Analysis. The frequency content of simulated responses is analyzed with three spectral analysis tools. A short-time Fourier transform—or STFT—provides the spectrum of signals [20]. To aid the interpretation, several elements have been superposed over the spectrograms: the eigenfrequencies of the respective free structures, the rotating speed harmonics with the highest amplitudes, and frequencies associated with main rays produced by modulations in the rotational speed.

The second tool is based on a two-dimensional discrete Fourier transform—2D DFT—which determines the spatial decomposition sorted by NDs for each spectrum frequency. An analysis of the complete spatial spectrum reveals the modal decomposition in forward (fw) participation and backward (bw) participation for a given diameter [2,9].

Finally, a combination of these two spectral analysis tools is used to better understand the ND or spatial content during the time the frequencies are present in the spectrum. This tool gives the frequency evolution versus time of a spatial filtered signal (STFT filtered on diameters).

The frequency analysis will be carried out over the range of initial bending modes [0–4000] Hz.

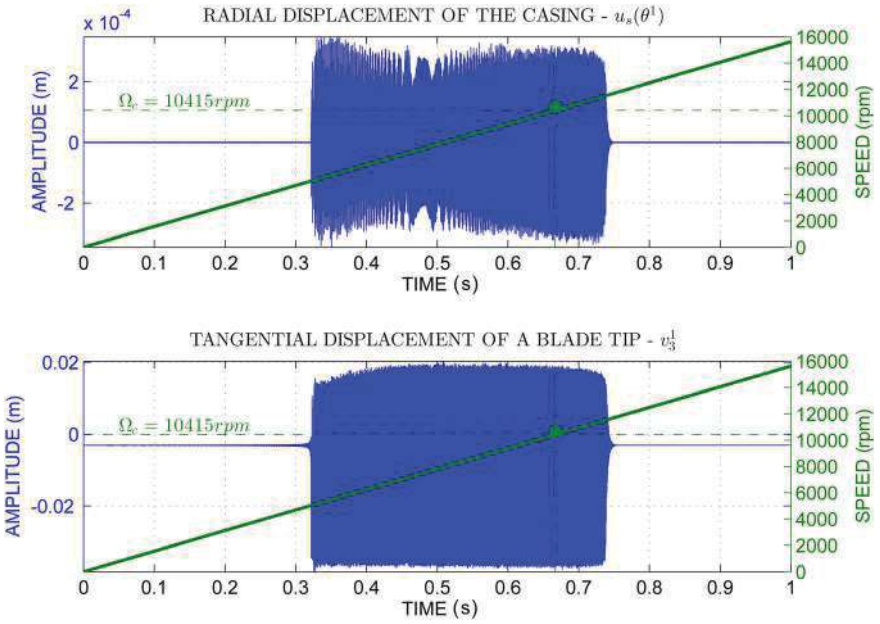

Fig. 9 Dynamic response of the casing (top) and the bladed disk (bottom) with a fast speed ramp for $\mu = 0.1$ and $k_w = 1 \times 10^{-12}$ Pa^{-1}

Frequency Versus Time Evolution. The time-frequency analysis (see Fig. 4) was applied to the tangential displacement of the blade tip and the radial displacement of the casing. The structure's responses show two different behaviors before and after $t \approx 2.78$ s. Before $t \approx 2.78$ s, the spectrogram displayed in Fig. 4(*a*) shows mainly the stator response to the external excitation introduced to initiate contact, at the frequency $f_{\text{excit}} = \omega_s^1$. We can also see the excitation frequency modulation by 12 times the rotational speed at $f_{\text{excit}} \pm 12\ \Omega$. It should be noticed that the number 12 is interpreted as two times the number of blades (Na), although this is not yet established as a generality in the paper. Frequency modulation by the rotating speed will be called sideband [9,21] in the remainder of this paper.

At the same time, the bladed disk spectrum illustrated in Fig. 4(*b*) is characterized by the frequency $\omega_s^1 + 2\,n_d^1\,\Omega$ (or $\omega_s^1 + n_d^1\,\Omega + \Omega$). This latter could be interpreted as a first-order sideband of the excitation frequency seen on the rotating frame. Moreover, the sidebands $\omega_s^1 + 6\,n_d^1\,\Omega$ and $\omega_s^1 - 2\,n_d^1\,\Omega$ are also present in the spectrogram. These sidebands are spaced by 4 Ω from $\omega_s^1 + 2\,n_d^1\,\Omega$. The expression of this modulation becomes $\omega_s^1 + 2\,n_d^1\,\Omega \pm 4\,\Omega$. This formula corroborates the observed beat period in the time response at the bottom of Fig. 3, where observed pulses are spaced by a characteristic period of $1/4\,\Omega$.

After $t \approx 2.78$ s when the amplitudes increase, three frequencies have the highest levels on the casing response given in Fig. 4(*a*). The first one (ω_s^1) is identified in time by a black-dotted line (■■■■■) superposed on the spectrogram. The second one is close to the casing mode with 2ND. Finally, the third frequency ($\omega_s^1 + 12\,\Omega$) is identified by a green-dotted line (■■■■■). Note that we keep the nomenclature of the natural frequencies to name the components of the spectrum, even if the frequencies of these components fluctuate near the natural frequencies. For example, the frequency of the component that fluctuates around 1700 Hz is denoted ω_s^1. So, the third main component of the bladed disk spectrum could be seen as a $12\,\Omega$ order sideband of ω_s^1.

At the same time ($t > 2.78$ s), on the bladed disk side—Fig. 4(*b*)—the frequency response is dominated by the components $\omega_s^1 + 2\,n_d^1\,\Omega$ (■■■■■) and $\omega_s^2 + 2\,n_d^2\,\Omega$ (■■■■■). The dotted lines displayed in Fig. 4(*b*) and denoted by $\omega_s^i + 2\,n_d^i\,\Omega$ were obtained from the identification of the main frequency on the stator spectrum (Fig. 4(*a*)) added to $2\,n_d^i\,\Omega$ ($i = 1,\ 2$). In other words, the spectrum of the two structures is related by the factor $2\,n_d^i$.

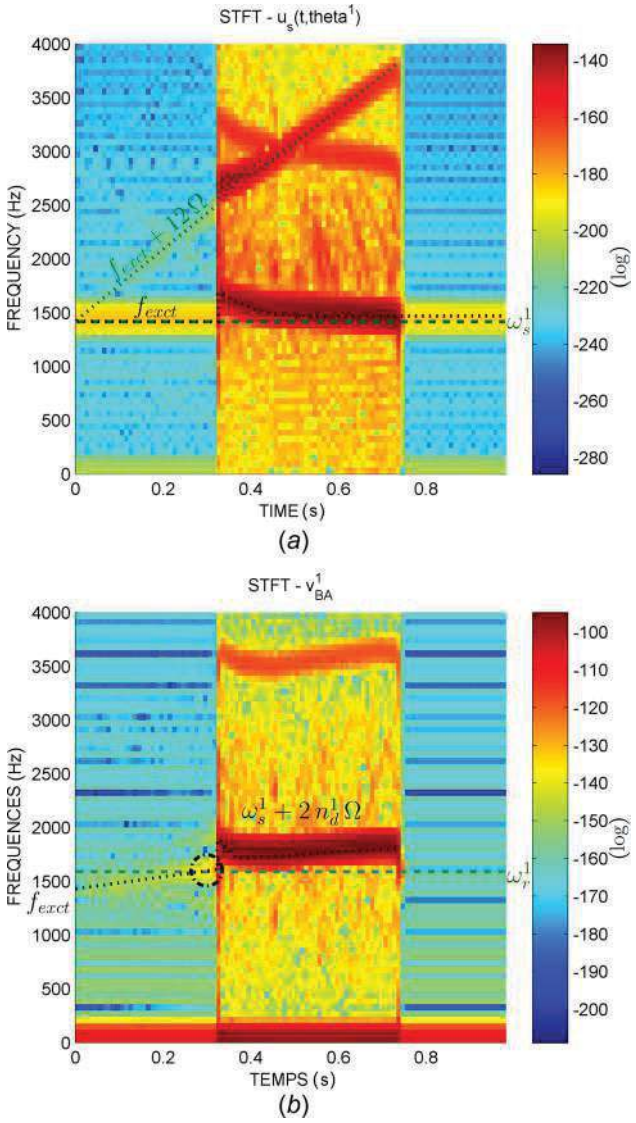

Fig. 10 STFT of the radial displacement of the casing and the tangential displacement of a blade tip with a fast speed ramp for $\mu = 0.1$ and $k_w = 1 \times 10^{-12}\,\text{Pa}^{-1}$: (*a*) casing and (*b*) bladed disk

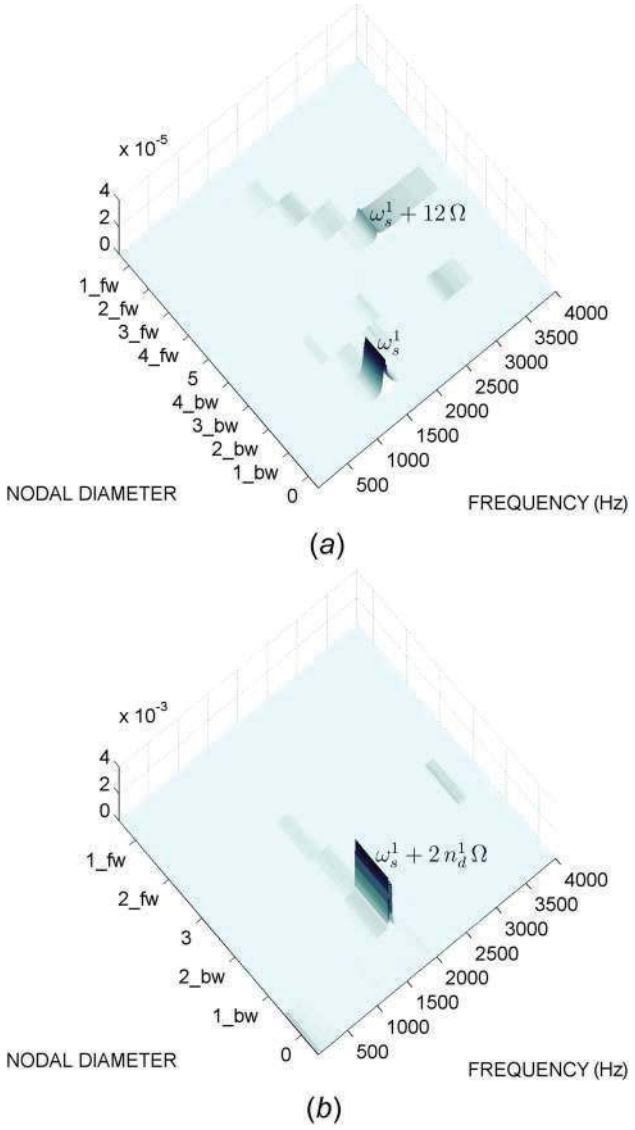

Fig. 11 Two-dimensional DFT diagram of the first family of modes of both structures during the burst. Simulation computed with a fast speed ramp for $\mu = 0.1$ and $k_w = 1 \times 10^{-12}\,\text{Pa}^{-1}$: (*a*) casing and (*b*) bladed disk.

Frequency Versus Spatial Content. The next step of this frequency analysis is performed with a 2D DFT applied to a set of sensors equally spaced on both structures [2,9]. At $t < 2.78$ s, the frequency–ND diagram shown in Fig. 5(*a*) indicates that a stationary wave with 1ND at $f_{\text{exct}} = 1417$ Hz is indeed present, while the bladed disk response is dominated by a backward wave with 1ND at $\omega_s^1 + 2\,n_d^1\,\Omega$. By looking at the full spatial spectrum, the diagram can reveal the NDs mainly responding together with the amplitudes of the associated forward and backward components. In this case, the frequency of the bladed disk and the stator is not related in the usual way—Eq. (13). Nevertheless, the first family mode of the bladed disk with 1ND seems to be excited by frequency $\omega_s^1 + 2\,n_d^1\,\Omega$ (see black dashed–dotted circle on Fig. 4(*b*)). This could be interpreted as a coincidence between a component of the casing vibration as perceived from the rotating frame and a bladed disk mode with the same number of NDs

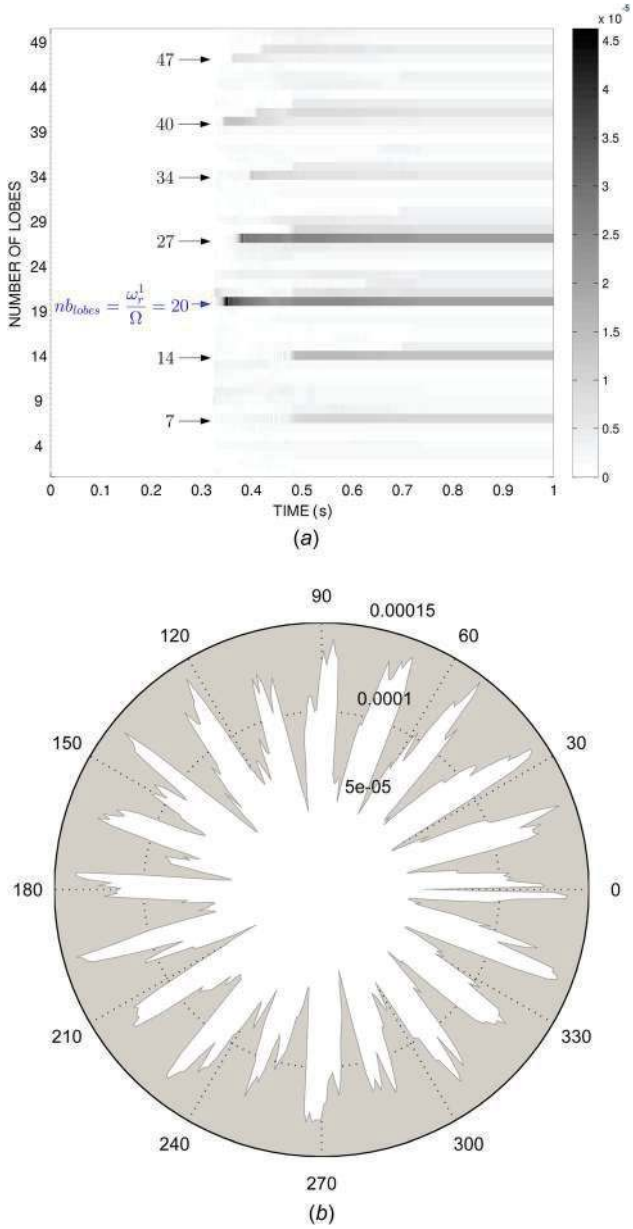

Fig. 12 Wear pattern analysis of the abradable coating for a simulation with a fast speed ramp for $\mu = 0.1$ and $k_w = 1\times10^{-12}$ Pa^{-1}: (*a*) time history of wear patterns and (*b*) wear map at the beginning of the burst

$$\omega_s^1 + 2\,n_d^1\,\Omega = \omega_r^1 \tag{14}$$

However, as said before, the component $\omega_s^1 + 2\,n_d^1\,\Omega$ may be interpreted as a sideband of the casing response seen on the rotating frame, which implies a frequency and spatial coincidence between this sideband and a bladed disk mode with 1ND

$$\underbrace{\omega_s^1 + n_d^1\,\Omega}_{\text{casing mode observed from the rotating frame}} \quad + \quad n_d^1\,\Omega \quad = \quad \omega_r^1$$

After this coincidence, the amplitudes of vibration of both structures increase and their spatial contents change. In Fig. 6(*a*), a 2ND backward mode is observed on the casing, along with a 1ND backward traveling wave with a lower amplitude compared to the previous mode. On the bladed disk, a 1ND backward mode (whose frequency follows the $\omega_s^1 + 2\,n_d^1\,\Omega$ relationship) produces the highest amplitude, as shown in Fig. 6(*b*).

In this case and viewing the factors discussed before, we cannot establish the presence of a modal interaction between the two structures. However, as said above, the burst seems to be initiated by a frequency and spatial coincidence between a sideband of the casing, as perceived on the rotating frame and a natural frequency of the bladed disk.

Frequency and Spatial Content Evolution Versus Time. The proposed approach is supplemented by a "before and after" analysis of the evolution of the spatial and frequency content during the two structures' response times. The STFTs filtered on NDs displayed in Figs. 7 and 8 make it possible to identify the spatial content of all the components found in the spectrograms. Table 1 summarizes the results of these analyses.

The ND filtering on the casing is obtained directly by plotting the STFTs of the A^{n_d} coefficients—see Eq. (2). Figure 7(*a*) confirms that the frequency superposed by a black-dotted line (■■■■■) on the casing spectrogram (Fig. 7(*a*)) has a spatial content of 1ND. The STFT of the coefficient A^2 given in Fig. 8(*a*) shows the 2NDs excitation during the burst, the harmonic 12 of the rotating speed (12 Ω), the second harmonic of excitation frequency ($2\,f_{\text{exct}}$), and its sidebands ($2\,f_{\text{exct}} \pm 12\,\Omega$).

Following this analysis for all the A^{n_d} coefficients of the stator, one could easily identify the spatial content present in the casing spectrum.

The same analysis was performed using the tangential displacements of the blade tips. The spatial content is dominated by 1ND contribution at the frequency $\omega_s^1 + 2\,n_d^1\,\Omega$ (■■■■■) as confirmed by the STFT filtered on diameter one (see Fig. 7(*b*)). Sidebands $\omega_s^1 - 2\,n_d^1\,\Omega$, $\omega_s^1 \pm 10\,n_d^1\,\Omega$ and $\omega_s^1 \pm 14\,n_d^1\,\Omega$ are also found in the same spectrogram. The response of frequency $\omega_s^2 + 2\,n_d^2\,\Omega$ (■■■■■) has a spatial content with 2NDs, as depicted in Fig. 8(*b*). On the same figure, one can observe the sidebands $2\,\omega_s^1 \pm 4\,\Omega$ and $2\,\omega_s^1 \pm 8\,\Omega$ of the second harmonic of excitation frequency and the fourth harmonic (4 Ω) and eighth harmonic (8 Ω) of the rotational speed.

This analysis makes it possible to clearly relate the spatial and frequency contents of both structures. At $t < 2.78$ s, the excitation frequency and its sidebands $f_{\text{exct}} \pm 12\,\Omega$ are visible on the filtered diagrams when the odd diameters are kept. On the other hand, the harmonic 12 of the rotating speed (12 Ω), the second harmonic of excitation frequency ($2\,f_{\text{exct}}$), and its sidebands ($2\,f_{\text{exct}} \pm 12\,\Omega$) appear on the even index of the spatial spectrum.

On the bladed disk, the sidebands $\omega_s^1 \pm 2\,\Omega \times (2p+1)$ and $2\,f_{\text{exct}} \pm 2\,\Omega \times (2p)$ are given, respectively, by odd NDs with $p \in \{0, 1, 2, 3\}$ and even NDs with $p \in \{1, 2\}$. Harmonic four (4 Ω) and eight (8 Ω) of the rotating speed are observed for even diameters.

The spectral analysis highlighted the presence of many sidebands and harmonics of the rotating speed, which can be explained by the contact nonlinearity between rotating and stationary parts [9]. When these terms coincide with the natural

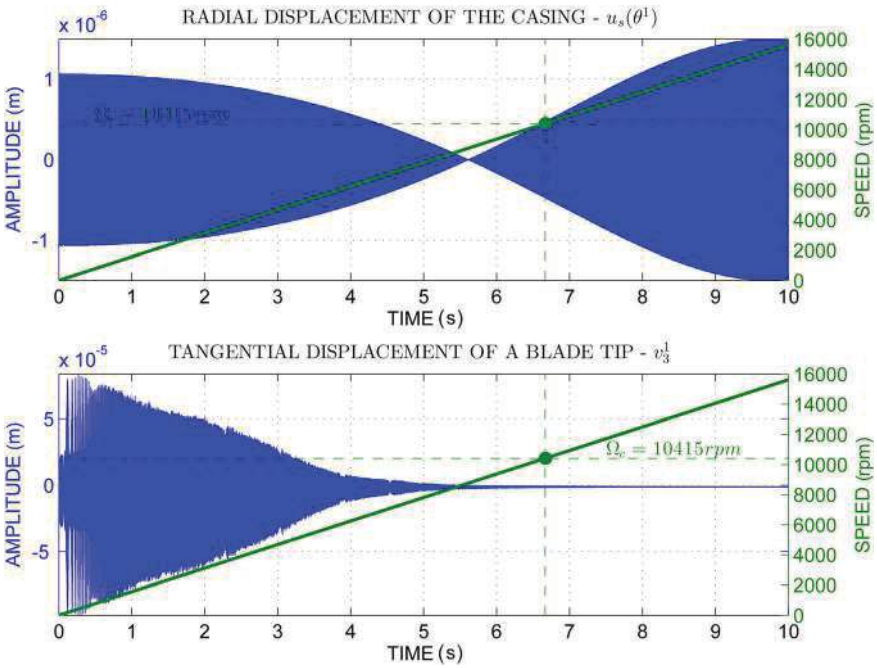

Fig. 13 Dynamic response of the bladed disk (top) and the casing (bottom) with a slow speed ramp for $\mu = 0.1$ and $k_w = 1\times10^{-12}$ Pa^{-1}

frequencies of the structures, the amplitudes increase and may lead to a burst of vibration.

The impact of rotational acceleration has been tested but no influence has been observed in this case. This is no longer verified when wear is introduced.

Dynamic Behavior With Friction and Wear

This section focuses on the influence of wear on the dynamic behavior in a situation of blade-to-casing contact. The simulations were carried out with a friction coefficient $\mu = 0.1$ and an Archard's wear coefficient $k_w = 1 \times 10^{-12}$ Pa^{-1}. The introduction of wear reveals two behaviors depending on the slope of the speed ramp (the speed range is the same for all the simulations). The first case, referred to as "fast speed ramp," uses a speed ramp with a rise time of $t = 1$ s. The second case, referred to as "slow speed ramp," uses a rise time of $t = 10$ s.

Fast Speed Ramp. In this case, the dynamic response of the system shown in Fig. 9 is characterized by a simultaneous increase in amplitude on both structures for $t = [0.32–0.75]$ s, which corresponds to the speed range $\Omega = [5000–11{,}700]$ rpm. Here again, it is important to note that the burst is initiated below the critical theoretical speed Ω_c. Vibrations disappear after $t = 0.75$ s, when the abradable material is removed by the wear process as shown below; hence, the clearance between the casing and blade tips is increased.

The spectrogram of the radial displacement of the casing highlights the main frequencies present in the previous simulation without wear. The black-dotted line (■■■■■) in the casing spectrogram of Fig. 10(*a*) tracks a frequency component about 1500 Hz which corresponds to a spatial content with 1ND. Before and after the burst, this frequency coincides with the excitation frequency f_{excit}, whereas during the burst it has a higher value which decreases with time. This seems to be accompanied by a 12 Ω (or 2 $Na\Omega$) sideband, which is also present in the spectrum. Its frequency follows the relation $f_{\text{excit}} + 12\ \Omega$ and was indicated by a green-dotted line (■■■■■).

The 2D DFT diagram computed during the burst (see Fig. 11(*a*)) makes it possible to confirm the nature of the response which is a 1ND backward wave (■■■■■).

The spectrogram of the tangential displacement of the bladed disk—Fig. 10(*b*)—shows a frequency component following the relation $\omega_s^1 + 2\,n_d^1\,\Omega$ (■■■■■). Around 3500 Hz, one can also see the second-order harmonic of this frequency. As in the case presented in the simulation without wear, the coincidence between the component following the relation $\omega_s^1 + 2\,n_d^1\,\Omega$ and the natural frequency of the bladed disk with 1ND (ω_r^1) seems to initiate the burst of vibration on both structures. The 2D DFT diagram of the bladed disk computed during the burst (Fig. 11(*b*)) is dominated by a 1ND forward mode. Note that on both structures, the two waves have the same number of NDs and travel in the same direction with the particularity that the propagation speeds are related by a 2 Ω instead of Ω as in the classical relation (13).

At the end of the burst, the absence of response on the bladed disk spectrum indicates that the contact is lost, this is confirmed by the analysis of the gap between the two structures (not presented here). Finally, it is important to note that the spectrograms presented in this section (Fig. 10) are less rich, in terms of spectral content, than those described in the simulation without wear (see Fig. 4).

The abradable material removed by the wear process stops the contact between the blade tips and the casing. STFT applied to the wear profile displayed in Fig. 12(*a*) indicates an increase in the intensity of wear at the beginning of the burst. At this time, the maximum wear depth is reached with 20 worn lobes (see the corresponding wear profile of the abradable coating pictured in Fig. 12(*b*)). As in Ref. [2], this number corresponds to the ratio between the first family mode of the bladed disk with 1ND and the rotational speed Ω

$$nb_{\text{lobes}} = \frac{\omega_r^1}{\Omega} = 20 \tag{15}$$

The previous equation could be considered as a particular case of Eq. (13), where the natural casing frequency is a static shape ($\omega_s = 0$), and the number of ND is equal to the number of lobes ($n_d = nb_{\text{lobes}}$). The same behavior was found with only one overlong blade in contact with the casing [3,4,22]. In our case, all the blades are in contact. This can be verified by looking at the spaced lines every 6–7 units on the time history of the wear profile

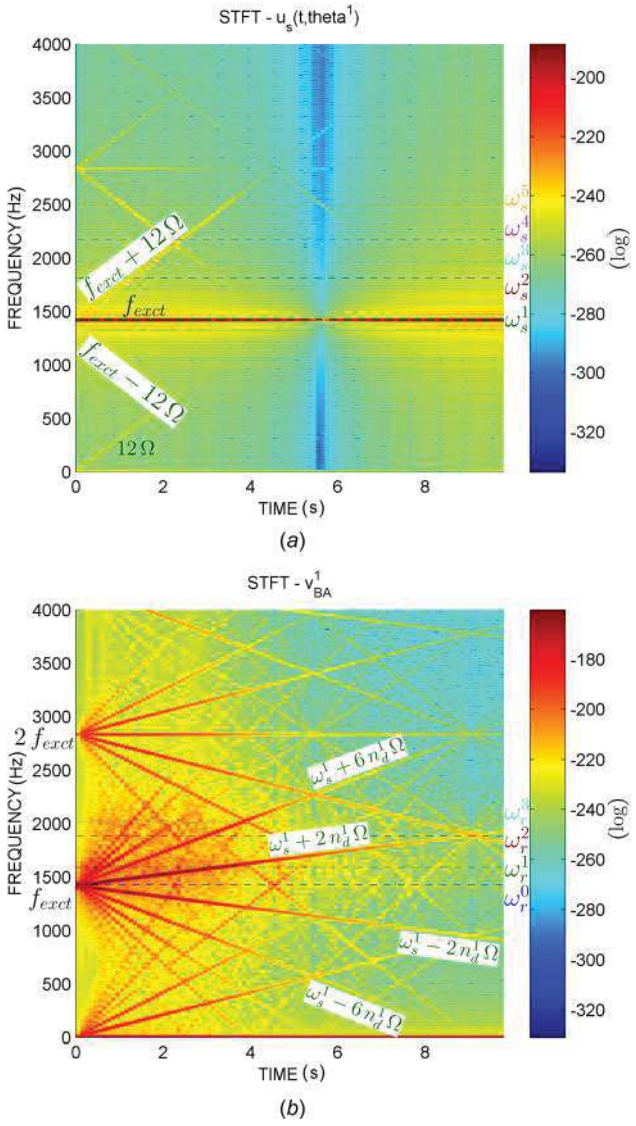

Fig. 14 STFT of the radial displacement of the casing and the tangential displacement of a blade tip with a slow speed ramp for $\mu = 0.1$ and $k_w = 1\times10^{-12}$ Pa^{-1}: (*a*) casing and (*b*) bladed disk

(Fig. 12(*a*)), which may be interpreted as the spatial modulation of the pattern with 20 lobes by the number of blades ($Na = 6$).

Slow Speed Ramp. In this section, we will compare the previous results to the results obtained with a slow speed ramp. The influence of the slope of the speed ramp is clearly demonstrated by comparing Figs. 9 and 13. The dynamic response of the system with a fast speed ramp exhibits an increase in amplitude after $t \approx 2.78$ s. Conversely, with a slow speed ramp, the amplitudes of both structures remain 2 order of magnitudes lower than the previous case, and in the case of the bladed disk, it decreases with time.

The casing spectrum given in Fig. 14(*a*) exposes the same main frequency (f_{excit}), sidebands ($f_{\text{excit}} \pm 12$ Ω), and rotational speed harmonic (12 Ω) with respect to the simulation without wear before the burst. In contrast, the frequency response of the bladed disk is characterized by the sidebands $\omega_s^1 \pm 2\, n_d^1\, \Omega$, $\omega_s^1 \pm 6\, n_d^1\, \Omega$, the second-order sidebands of the excitation frequency $2\,\omega_s^1 \pm 2\, n_d^1\, \Omega$, and $2\,\omega_s^1 \pm 6\, n_d^1\, \Omega$. The fourth harmonic (4 Ω) and eighth harmonic (8 Ω) of the rotational speed are also found. The amplitude of these terms will gradually decrease over time. When the slow

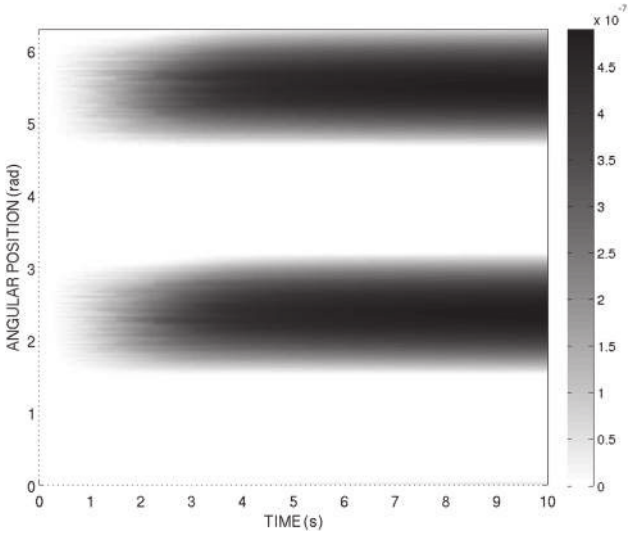

Fig. 15 Time history of wear patterns of the abradable coating for a simulation with a slow speed ramp for $\mu = 0.1$ and $k_w = 1\times10^{-12}$ Pa^{-1}

ramp is introduced, the abradable coating is consumed ten times faster since the bladed disk achieved ten times more revolutions than the simulation with the fast speed ramp. The gap is therefore higher when it reaches the time when Eq. (14) is verified. It is believed that the updated gap is then sufficient to prevent the burst.

The wear map shown in Fig. 15 indicates that contact occurs in two diametrically opposite locations. This map corresponds to a two-lobe wear profile [9].

Conclusion

A blade-to-casing simulation with a simplified finite element model of a rotating bladed disk and a flexible casing was presented in this paper. A mathematical formulation of an elastodynamic contact with friction (Coulomb's law) and wear (Archard's law) was derived for this application. Contact was initiated by a dynamic excitation of the stator. The first simulation analyzed showed the dynamic behavior of the system when the friction is taken into account. The amplitudes of vibration of both structures increased when the condition $\omega_s^1 + 2\, n_d^1\, \Omega = \omega_r^1$ was fulfilled. This may be interpreted as the coincidence between the frequency of a mode with 1ND on the rotor (ω_r^1) and a sideband of the frequency of a mode with 1ND on the stator (ω_s^1), which is equal to $\omega_s^1 + 2\,\Omega$ when seen in the rotating frame.

The introduction of wear into the system changed the dynamic behavior of both structures by adding a speed sensitivity. Two different behaviors depending on the slope of the speed ramp were found. With a fast speed ramp, the displacement amplitudes of the two structures increased to very high values until the removal of the abradable coating stopped the process. At the beginning of the burst, the abradable material was worn in a specific pattern. The number of lobes corresponded to the ratio between the mode frequency and the rotating speed. The introduction of a slow speed ramp prevented the burst of vibration on both structures because the abradable coating was consumed faster, the bladed disk achieving more revolutions. In that particular case, all of the abradable material was completely worn before it had reached the critical speed.

Acknowledgment

This work was partially funded by the French National Research Agency (ANR), within the framework of its COSINUS

Technological Research Program (IRINA project, ref. ANR 09 COSI 008 01 IRINA).

Nomenclature

$\mathbf{C_N}$ = linearized vector yielding the normal force direction
$\mathbf{C_T}$ = linearized vector yielding the tangential force direction
$\mathbf{D}$ = structural damping matrix
DTF = discrete Fourier transform
$\mathbf{F_c}$ = contact forces vector
$\mathbf{F_{ext}}$ = external forces vector
g = distance function
$\mathbf{g}$ = initial gap vector
$\mathbf{K}$ = stiffness matrix
k_w = Archard's law wear coefficient
$\mathbf{M}$ = mass matrix
n_d = number of nodal diameters
ND = nodal diameter
P_N = normal contact pressure
STFT = short-time Fourier transform
$\mathbf{u}$ = displacement vector
u_s = radial displacement at the middle plane of the elastic ring
$\mathbf{w}$ = wearing depth vector
w_s = tangential displacement at the middle plane of the elastic ring
θ = angular coordinate around the elastic ring
λ_N = Lagrange multiplier
μ = coefficient of friction
Ω = bladed disk speed
Ω_c = critical modal interaction speed
$\omega_r^{n_d}$ = natural frequency of the bladed disk mode with n_d nodal diameters
$\omega_s^{n_d}$ = natural frequency of the casing mode with n_d nodal diameters

References

[1] Jacquet-Richardet, G., Torkhani, M., Cartraud, P., Thouverez, F., Baranger, T. N., Herran, M., Gibert, C., Baguet, S., Almeida, P., and Peletan, L., 2013, "Rotor to Stator Contacts in Turbomachines. Review and Application," Mech. Syst. Signal Process., **40**(2), pp. 401–420.

[2] Almeida, P., Gibert, C., Thouverez, F., Leblanc, X., and Ousty, J.-P., 2014, "Experimental Analysis of Dynamic Interaction Between a Centrifugal Compressor and Its Casing," ASME J. Turbomach., **137**(3), p. 031008.

[3] Millecamps, A., Brunel, J.-F., Dufrenoy, P., Garcin, F., and Nucci, M., 2009, "Influence of Thermal Effects During Blade-Casing Contact Experiments," ASME Paper No. DETC2009-86842.

[4] Batailly, A., Legrand, M., Millecamps, A., and Garcin, F., 2012, "Numerical-Experimental Comparison in the Simulation of Rotor/Stator Interaction Through Blade-Tip/Abradable Coating Contact," ASME J. Eng. Gas Turbines Power, **134**(8), p. 082504.

[5] Strömberg, N., 1999, "Finite Element Treatment of Two-Dimensional Thermo-elastic Wear Problems," Comput. Methods Appl. Mech. Eng., **177**(3–4), pp. 441–455.

[6] Salles, L., Blanc, L., Thouverez, F., Gouskov, A., and Jean, P., 2012, "Dual Time Stepping Algorithms With the High Order Harmonic Balance Method for Contact Interfaces With Fretting-Wear," ASME J. Eng. Gas Turbines Power, **134**(3), p. 032503.

[7] Archard, J. F., 1953, "Contact and Rubbing of Flat Surfaces," J. Appl. Phys., **24**(8), pp. 981–988.

[8] Williams, R., 2011, "Simulation of Blade Casing Interaction Phenomena in Gas Turbines Resulting From Heavy Tip Rubs Using an Implicit Time Marching Method," ASME Paper No. GT2011-45495.

[9] Almeida, P., Gibert, C., Thouverez, F., and Ousty, J.-P., 2014, "On Some Physical Phenomena Involved in Blade-Casing Contact," 9th International Conference on Structural Dynamics, Porto, Portugal, June 30–July 2, pp. 2063–2071.

[10] Lesaffre, N., Sinou, J.-J., and Thouverez, F., 2007, "Contact Analysis of a Flexible Bladed-Rotor," Eur. J. Mech.-A/Solids, **26**(3), pp. 541–557.

[11] Love, A. E. H., 1906, *A Treatise on the Mathematical Theory of Elasticity*, Cambridge University Press, New York.

[12] Lesaffre, N., 2007, "Stabilité et analyse non-linéaire du contact rotor-stator," Ph.D. thesis, Ecole Centrale de Lyon, Lyon, France.

[13] Carpenter, N. J., Taylor, R. L., and Katona, M. G., 1991, "Lagrange Constraints for Transient Finite Element Surface Contact," Int. J. Numer. Methods Eng., **32**(1), pp. 103–128.

[14] Legrand, M., 2005, "Modèles de prédiction de l'interaction rotor/stator dans un moteur d'avion," Ph.D. thesis, Ecole Centrale de Nantes, Nantes, France.

[15] Legrand, M., Pierre, C., Cartraud, P., and Lombard, J.-P., 2009, "Two-Dimensional Modeling of an Aircraft Engine Structural Bladed Disk-Casing Modal Interaction," J. Sound Vib., **319**(1–2), pp. 366–391.

[16] Salles, L., 2010, "Etude de l'usure par fretting sous chargements dynamiques dans les interfaces frottantes: Application aux pieds d'aubes de turbomachines," Ph.D. thesis, Ecole Centrale de Lyon, Lyon, France.

[17] Salles, L., Blanc, L., Thouverez, F., Gouskov, A., and Jean, P., 2009, "Dynamic Analysis of a Bladed Disk With Friction and Fretting-Wear in Blade Attachments," ASME Paper No. GT2009-60151.

[18] Salles, L., Blanc, L., Thouverez, F., and Gouskov, A., 2011, "Dynamic Analysis of Fretting-Wear in Friction Contact Interfaces," Int. J. Solids Struct., **48**(10), pp. 1513–1524.

[19] Schmiechen, P., 1997, "Travelling Wave Speed Coincidence," Ph.D. thesis, Imperial College of London, London, UK.

[20] Al-Badour, F., Sunar, M., and Cheded, L., 2011, "Vibration Analysis of Rotating Machinery Using Time-Frequency Analysis and Wavelet Techniques," Mech. Syst. Signal Process., **25**(6), pp. 2083–2101.

[21] Shmaliy, Y., 2006, *Continuous-Time Signals*, Springer, Dordrecht, The Netherlands.

[22] Millecamps, A., 2010, "Interaction aube-carter: Contribution de l'usure de l'abradable et de la thermomécanique sur la dynamique d'aube," Ph.D. thesis, Université de Lille 1, Lille, France.